Optics Letters

Inverse design of ultracompact multi-focal optical devices by diffractive neural networks

Yuyao Chen,[1] Yilin Zhu,[2] Wesley A. Britton,[2] and Luca Dal Negro[1,2,3,*]

[1]Department of Electrical and Computer Engineering and Photonics Center, Boston University, 8 Saint Mary's Street, Boston, Massachusetts 02215, USA
[2]Division of Materials Science and Engineering, Boston University, 15 Saint Mary's Street, Brookline, Massachusetts 02246, USA
[3]Department of Physics, Boston University, 590 Commonwealth Avenue, Boston, Massachusetts 02215, USA
*Corresponding author: dalnegro@bu.edu

Received 7 April 2022; revised 10 May 2022; accepted 12 May 2022; posted 12 May 2022; published 26 May 2022

We propose an efficient inverse design approach for multi-functional optical elements based on adaptive deep diffractive neural networks (a-D^{2}NNs). Specifically, we introduce a-D^{2}NNs and design two-layer diffractive devices that can selectively focus incident radiation over two well-separated spectral bands at desired distances. We investigate focusing efficiencies at two wavelengths and achieve targeted spectral line shapes and spatial point-spread functions (PSFs) with optimal focusing efficiency. In particular, we demonstrate control of the spectral bandwidths at separate focal positions beyond the theoretical limit of single-lens devices with the same aperture size. Finally, we demonstrate devices that produce super-oscillatory focal spots at desired wavelengths. The proposed method is compatible with current diffractive optics and doublet metasurface technology for ultracompact multispectral imaging and lensless microscopy applications.

https://doi.org/10.1364/OL.460186

Multifunctional diffractive optical elements (DOEs), when integrated atop on-chip detectors, enable ultracompact imaging functionalities for miniaturized flat cameras and microscopes [1–4]. Multispectral behavior is often achieved by partitioning single-layer devices into separate phase regions that affect different wavelengths. However, this design limits the maximum efficiency achievable at each wavelength, which is a significant challenge for DOEs working at multiple wavelengths [5,6]. This is because when one specific wavelength illuminates the entire device, only the phase region designed to operate at that wavelength will produce the desired output, while the other part of the illuminated device area will not, thus requiring a different approach.

To address this important challenge, we propose here novel multi-layer designs based on the flexibility of adaptive deep diffractive neural networks (a-D^{2}NNs) for the engineering of multi-layered diffractive devices with targeted spectral response and spatial point-spread functions (PSFs) at different wavelengths. Recently, deep diffractive neural networks (D^{2}NNs) that combine optical diffraction with deep learning capabilities have been reported and applied to all-optical diffraction-based systems that implement object recognition [7]. Moreover, D^{2}NNs have also been demonstrated successfully for the inverse design of multi-layered diffractive devices that achieve pulse shaping [8] and broadband filtering [9]. These devices are macroscopic, with typical dimensions up to a few centimeters and are fabricated using 3D printing for applications in the terahertz domain [8,9]. However, the design of diffractive devices that cover multiple spectral bands in the optical regime is very challenging and requires a more flexible implementation of the D^{2}NN platform.

In this paper, we introduce and utilize a-D^{2}NN that leverages an adaptive loss weight algorithm for the inverse design of two-layer, ultracompact, dual-band DOEs. The a-D^{2}NNs are trained to maximize the focusing efficiencies for λ_1 at f_1 and λ_2 at f_2. The engineered devices show efficiencies over 50% at both targeted wavelengths, exceeding the limit of phase-modulated single-layer DOEs [5,6,10]. We systematically investigate how the focusing efficiencies vary with the distance between the two diffractive layers and the pixel size, taking into account practical fabrication constraints. We also investigate how the efficiency is affected by the phase discretization level of the proposed diffractive devices. In addition, the obtained phase designs can also be implemented using current metasurface technology [1,11–13], including the recently developed doublet metasurface fabrication approach [14,15]. An important aspect of our approach is the design of the spectral line shapes of DOEs. In fact, we demonstrate dual-band devices with designed bandwidths that are narrower than diffractive lenses with the same aperture size. Finally, we show that a-D^{2}NNs can be implemented to design devices with desired spatial PSFs, including DOEs that produce super-oscillatory fields with focal spots below the diffraction limit [16].

Figure 1(a) illustrates the general two-layer diffractive device concept consisting of two diffractive phase plates located on both sides of a transparent substrate. The varying thickness profiles of the materials on the phase plates impart different phase shifts to the waves that propagate through the device. The design of the a-D^{2}NN that implements such a device is shown schematically in Fig. 1(b), where the two diffractive layers of the a-D^{2}NN correspond to the two phase plates of the device. We implement the Rayleigh–Sommerfeld (RS) first integral formulation within the a-D^{2}NN in order to simulate the forward light propagation from one plane to the next one, according to the model

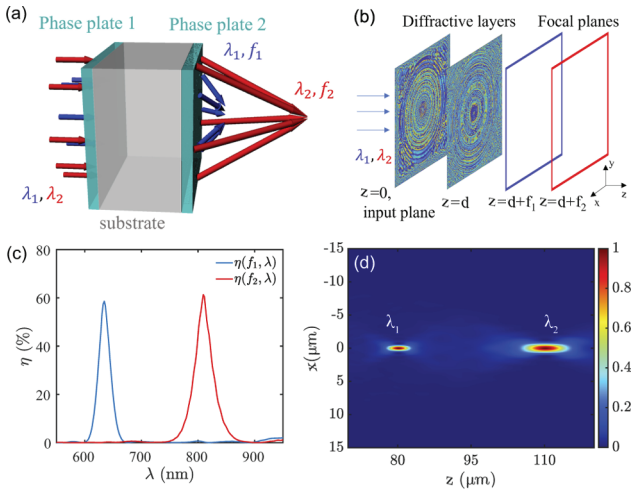

Fig. 1. (a) Two-layer dual-band DOE and (b) D^{2}NN representation. (c) Focusing efficiency spectra for the device in (a) with a-D^{2}NN. (d) Side view of normalized diffraction intensity at λ_1 and λ_2.

[2,10]:

$$A_o(x', y') = A_s(x, y) * h(x, y; x', y'; z, k) \quad (1)$$

$$h(x, y; z, k) = \frac{1}{2\pi}\frac{z}{r}\left(\frac{1}{r} - jk\right)\frac{e^{jkr}}{r}, \quad (2)$$

where $*$ denotes the two-dimensional spatial convolution and A_o, A_s are the transverse field distributions on the source and observation plane with coordinates (x, y) and (x', y'), respectively. Moreover, $k = 2\pi n/\lambda$ is the wavenumber, where λ is the incident wavelength in vacuum and n is the index of medium between the two planes. We use $r = \sqrt{x^2 + y^2 + z^2}$, where z is the distance between the two planes. In our two-layer DOE, we first compute the forward propagation from plane $z = 0$ to plane $z = d$ at wavelengths λ_1 and λ_2. Then the field distributions on the focal plane for λ_1 at $z = d + f_1$ and for λ_2 at $z = d + f_2$ are calculated. We then utilize the a-D^{2}NN to maximize the focusing efficiency η at these two focal planes, using the following definition for the focusing efficiency [10]:

$$\eta(\lambda, z) = \frac{\int_0^{2\pi}\int_0^{3\mathrm{FWHM}/2} I'(\lambda, z, \rho', \theta')\, dr' d\theta'}{\iint I(\lambda, z = 0, \rho, \theta) dS}, \quad (3)$$

where I' denotes the intensity distribution on the focal plane, I denotes the intensity distribution on the input plane, and S denotes the input plane aperture. The symbols (ρ, θ) and (ρ', θ') are the polar coordinates on the focal and input plane, respectively.

The focusing efficiency is utilized in the loss function of the a-D^{2}NN as

$$\mathcal{L} = w_1(1 - \eta_1)^2 + w_2(1 - \eta_2)^2, \quad (4)$$

where $\eta_1 = \eta(\lambda_1, d + f_1)$, $\eta_2 = \eta(\lambda_2, d + f_2)$, and w_1 and w_2 are the loss weights. Based on the definition of a suitable loss function, the a-D^{2}NN is directly trained using error backpropagation within the diffractive layers without the need of training datasets. Therefore, the a-D^{2}NN achieves a more efficient inverse design of complex phase devices compared with data-driven neural network approaches [17,18]. Specifically, a-D^{2}NNs are trained by varying the phase profiles of the two diffractive layers in order to minimize $\mathcal{L}$. We train the latent variable h_ℓ on each pixel of the diffractive layers related to the material thickness h by $h = h_{\max}(\sin(h_\ell) + 1)/2$, where $h_{\max}$ is the specified maximum thickness of the device. The phase profile $\phi(x, y)$ induced by diffractive layers at wavelength λ is $\phi = 2\pi(n - 1)h/\lambda$. As a proof of concept, we select $\lambda_1 = 632.8$ nm, $\lambda_2 = 808$ nm, $f_1 = 80$ μm, and $f_2 = 110$ μm, which were used in our previous work [10]. The two diffractive layers are square apertures with $L = 100$ μm side length and the device pixel size is $\Delta x = 200$ nm. We assume that the substrate index $n = 3$, $h_{\max} = 500$ nm, and thickness $d = 200$ μm. Differently from the usual D^{2}NN approach, here we implement adaptive loss weights that balance the interplay between different loss terms automatically depending on their values [19,20]. In particular, we apply the following updates for $w_m (m = 1, 2)$ at the kth epoch of training:

$$w_m^k \leftarrow w_m^{k-1} + \gamma(1 - \eta_m)^2, \quad (5)$$

where γ is the learning rate for loss weights update and we choose $\gamma = 1$. We use a desktop with GeForce GTX 1080 Ti graphical processing unit (GPU, Nvidia Inc.), an Intel i7-8700K central processing unit (CPU, Intel Inc.) and 32 GB of RAM for training. We trained the a-D^{2}NN over 2000 epochs using an Adam optimizer with learning rate equal to 0.1. The typical training time is only ~10 min. In Fig. 1(c), we show the obtained focusing efficiency spectra of the device at f_1 and f_2. Specifically, we observe that $\eta(f_1, \lambda)$ and $\eta(f_2, \lambda)$ are peaked at λ_1 and λ_2, respectively, and that both η_1 and η_2 values exceed 50%. Therefore, the designed two-layer dual-band device exceeds the efficiency limit expected in a single-layer DOE. Moreover, in Fig. 1(d), we display the side view of the normalized intensity diffraction of the device, clearly showing that the two targeted wavelengths λ_1 and λ_2 are well focused at the designed focal lengths f_1 and f_2, respectively.

We further investigate the influence of the distance d between the two diffractive layers, while keeping all the other parameters as specified previously. The obtained values of η_1 and η_2 for devices with different d are shown in Fig. 2(a), which demonstrates that, for all the devices, the values of η_1 and η_2 remain above 50%. We next consider the discretization of the obtained continuous phase profiles into discrete levels used for scalable lithographic fabrication [2,10]. Figure 2(b) displays how the number of discretized levels of the device affect η_1 and η_2. In particular, we find that η_1 and η_2 increase with the number of phase levels used, with a similar scaling to the one reported for the diffraction efficiency of multi-level gratings [21]. In particular, we observe that our two-layer device can achieve $\eta_1 = 46\%$ and $\eta_2 = 52\%$ when only eight discretization levels are used. The

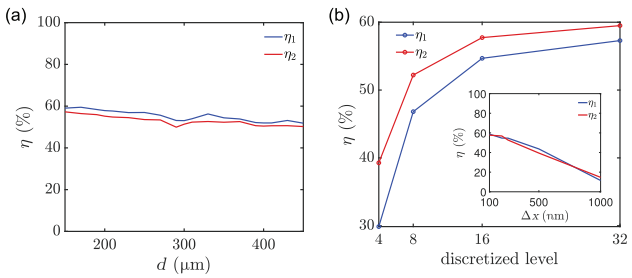

Fig. 2. (a) Focusing efficiency with respect to distance d between the two diffractive layers. (b) Focusing efficiency with respect to number of discrete phase levels. The inset shows the dependence of the focusing efficiencies on the pixel size (minimum spatial feature of the phase profile).

inset of Fig. 2(b) displays the focusing efficiency with respect to the pixel size Δx. Devices with smaller Δx achieve larger η_1 and η_2 efficiencies as they accommodate faster phase variations. Therefore, our analysis indicates that the proposed devices can be conveniently engineered using current multi-level DOE technology [2,10] as well as planar metasurfaces that provide nanoscale phase resolution (50–300 nm) [1,11,12,14].

Another important advantage of the DOE design based on a-D^{2}NNs is that we can engineer spectral line shapes by modifying the loss function used for training the network. To demonstrate this capability, we train a-D^{2}NNs to obtain devices with spectral line shapes for the focusing efficiency $\eta_{tm}(f_m, \lambda)$ $(m = 1, 2)$ described by

$$\eta_{tm}(f_m, \lambda) = \exp\left[-4\log(2)\left(\frac{\lambda - \lambda_m}{\sigma_m}\right)^2\right] \quad (m = 1, 2), \tag{6}$$

where λ_m and σ_m $(m = 1, 2)$ are the center wavelength and FWHM of the targeted Gaussian spectral line shape, respectively. We modify the loss function in the a-D^{2}NN as

$$\mathcal{L} = \sum_{m=1,2}\sum_{k=1}^{N} w_m(1 - \eta_m)^2 + \frac{1}{N} w_{sm}\left[\eta_m * \eta_{tm}(f_m, \lambda_k^m) - \eta_m(f_m, \lambda_k^m)\right]^2, \tag{7}$$

where $w_{sm}(m = 1, 2)$ is the loss weight for the spectral line shape loss term. The first term is the same used in Eq. (4). For the second term, we sample N discrete wavelengths of the target spectrum uniformly from $\lambda_{\min}^m$ to $\lambda_{\max}^m$ centered at $\lambda_m(m = 1, 2)$ and evaluate the focusing efficiencies over these wavelengths. The mean squared error (MSE) between the obtained $\eta_m(f_m, \lambda_k^m)$ and the target line shape $\eta_{tm}(f_m, \lambda)$ with its maximum rescaled to η_m is then calculated. During the training process, we apply the adaptive loss weights for both w_m and w_{sm}. We train the a-D^{2}NN with the same parameters used to generate Fig. 1 and we fix $\sigma_1 = \sigma_2 = \sigma$. In particular, we sampled $N = 30$ wavelengths over two ranges between $\lambda_{\min}^m = \lambda_m - 3\sigma$ and $\lambda_{\max}^m = \lambda_m + 3\sigma$. The a-D^{2}NN is trained over 2000 epochs. We show the spectral results for the device trained using $\sigma = 10$ nm and $\sigma = 40$ nm in Figs. 3(a) and 3(b), respectively. Furthermore, in Fig. 3(c), we display how η_1 and η_2 vary for devices optimized with different σ. A sharp drop of focusing efficiency is observed when the width of the targeted Gaussian line shape is decreasing below

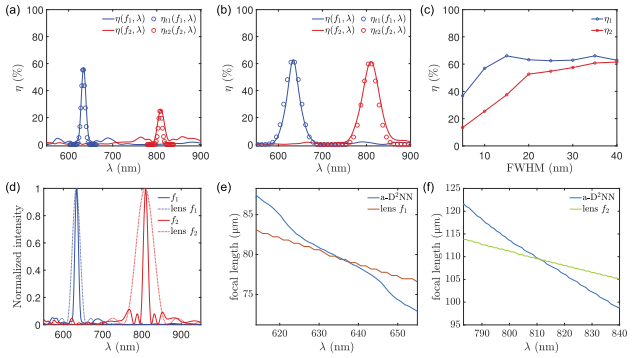

Fig. 3. Spectral line shapes with (a) $\sigma = 10$ nm and (b) $\sigma = 40$ nm. (c) η_1 and η_2 with respect to σ. (d) Normalized field intensity spectra for $\sigma = 10$ nm at f_1 (solid blue) and f_2 (solid red) compared with single diffractive lenses with focus λ_1 at f_1 (dashed blue) and λ_2 at f_2 (dashed red). (e), (f) Wavelength dependence of focal lengths around λ_1 and λ_2, respectively.

20 nm. We also evaluate the normalized field intensity spectra at the origin of focal planes at f_1 and f_2 for the device with $\sigma = 10$ nm. We compare our results with those of two diffractive lenses with the same dimension that focus λ_1 at f_1 and λ_2 at f_2. The analytical expression for the normalized intensity spectrum $I_m(\lambda)$ of a diffractive lens that focuses λ_m at f_m $(m = 1, 2)$ is given by [22]

$$I_m(\lambda) = \left[\frac{\sin(u_m(\lambda)/4)}{u_m(\lambda)/4}\right]^2, \tag{8}$$

where we defined

$$u_m = \frac{2\pi}{\lambda}\left(\frac{L}{2}\right)^2\left(\frac{\lambda}{f_m\lambda_m} - \frac{1}{f_m}\right).$$

As shown in Fig. 3(d), two-layer devices designed using the a-D^{2}NN method can feature significantly narrower bandwidths than diffractive lenses at both λ_1 and λ_2. Recalling that the intensity spectrum for a diffractive lens is completely determined once the parameters L, λ_m, and f_m are fixed, we appreciate that the designed two-layer DOEs provide the additional capability to tailor spectral line shapes for a given aperture size. To better understand how the obtained devices achieve narrow bandwidths, we evaluate the spectral dependence of their focal lengths near λ_1 and λ_2 and compare with diffractive lenses in Figs. 3(e) and 3(f), respectively. Our findings show that the focal lengths of the designed dual-band devices vary faster with respect to the wavelength than do in traditional diffractive lenses. Therefore, they can achieve enhanced spectral selectivity (narrower bandwidths), owing to their stronger defocusing behavior when varying the incident wavelengths.

We finally implement a-D^{2}NNs for the inverse design of two-layer DOEs with the desired focusing PSF. We model the PSF as a two-dimensional Gaussian function on the focal plane $f_m(m = 1, 2)$:

$$I_{tm}(x, y, z_m, \lambda_m) = \exp\left[-4\log(2)\left(\frac{x^2 + y^2}{(\alpha\epsilon_m)^2}\right)\right], \tag{9}$$

where $z_m = d + f_m$ is the focal plane z-coordinate for λ_m, α is a scaling constant that quantifies the degree of spatial localization of the designed focal spot with respect to the Rayleigh diffraction limit, which is achieved for $\alpha = 1$, and $\epsilon_m = 0.51\lambda_m f_m/L$ is the diffraction limited FWHM of the focal spot. To obtain the desired spatial PSFs, we implement the following loss function for training:

$$\mathcal{L} = \sum_{m=1,2}\sum_{x,y} w_m(1 - \eta_m)^2 + w_{pm}\left[I_m(0, 0, z_m, \lambda_m) * I_{tm}(x, y, z_m, \lambda_m) - I_m(x, y, z_m, \lambda_m)\right]^2, \tag{10}$$

where w_{pm} is the loss weight for the loss term of squared error between the device real PSF $I_m(x, y, z_m, \lambda_m)$ and the targeted PSF $I_{tm}(x, y, z_m, \lambda_m)$, with its maximum rescaled to $I_m(0, 0, z_m, \lambda_m)$. In particular, we trained an a-D^{2}NN using $\alpha = 0.4$, which corresponds to a FWHM below the diffraction limit. The intensity cuts through the center of the focal spots at λ_1 and λ_2 are shown in Figs. 4(a) and 4(b), respectively. The dashed lines are the targeted PSF used for training the network. The obtained intensity profiles indicate the formation of optical super-oscillations, which have been shown to result in arbitrarily small energy concentration without the assistance of evanescent waves [23,24]. We note that the obtained PSFs exhibit the presence of significant sidebands compared with the targeted Gaussian PSF. This

is due to the fundamental nature of super-oscillations in which enhanced (sub-diffractive) field focusing can only be achieved at the expense of a polynomial increase in the power directed into the sidebands [16]. Owing to their extreme localization properties, optical super-oscillations have found applications in sub-wavelength imaging and microscopy [25]. To demonstrate super-oscillations in our devices, we studied the phase gradient $|\nabla\phi|$ of the diffracted field on the focal plane, which corresponds to a local wavenumber. Super-oscillations form when $|\nabla\phi|>k_m$, where $k_m = 2\pi/\lambda_m$ $(m = 1, 2)$ are the incident wavenumbers. In Figs. 4(a) and 4(b), we display, for the two wavelengths of interest, the phase gradient profiles of the fields normalized by k_m. We notice that the peaks of $|\nabla\phi|/k_m$ exceed unity around the designed focal spots, demonstrating the super-oscillation character of the waves. We further show the two-dimensional focal intensity distributions and $|\nabla\phi|/k_m$ maps on the two different focal planes in Figs. 4(c) and 4(d) and Figs. 4(e) and 4(f), respectively. In Figs. 4(g) and 4(h), we summarize our results for the variation of focusing efficiencies with respect to the localization parameter α. We note that the focusing efficiencies

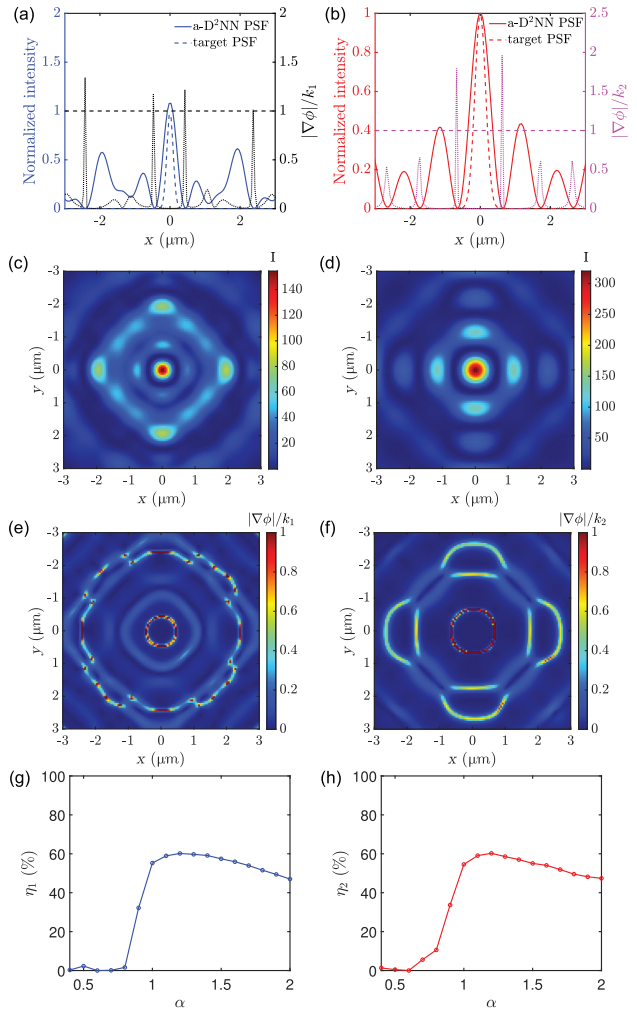

Fig. 4. (a) Normalized transverse intensities at λ_1 (blue solid line) and (b) at λ_1 (red solid line) and corresponding phase gradients across the focal spots. (c), (d) Focal plane intensity profiles at λ_1 and λ_2, respectively, with $\alpha = 0.4$. (e), (f) Normalized phase gradient maps at the focal planes for λ_1 and λ_2, respectively. For better visualization, the range of the color bars is limited to [0, 1]. (g), (h) η_1 and η_2 with respect to α.

slightly decrease with increasing α if $\alpha>1$, while they suddenly drop to almost zero for decreasing α when $\alpha<1$, consistently with the super-oscillating regime [23,24].

In conclusion, we introduced an inverse design approach for a dual-band multi-focal DOE based on flexible a-D^{2}NNs. We demonstrate novel two-layer designs that show $\eta_1, \eta_2>50\%$, beyond the limit of single-layer DOEs working at two wavelengths. Furthermore, we showed the designs of DOEs with desired spectral line shapes and FWHM down to $\sigma = 5$ nm. Finally, we show PSF engineering with designed super-oscillatory focal spots below the diffraction limit. The flexible approach introduced here enables the engineering of two-layer diffractive devices with desired spectral and spatial responses for multi-band imaging and microscopy applications.

Funding. National Science Foundation (ECCS-2015700).

Disclosures. The authors declare no conflicts of interest.

Data availability. Data underlying the results presented in this paper are not publicly available at this time but may be obtained from the authors upon reasonable request.

Supplemental document. See Supplement 1 for supporting content.

REFERENCES

1. S. Banerji, M. Meem, A. Majumder, F. G. Vasquez, B. Sensale-Rodriguez, and R. Menon, Optica **6**, 805 (2019).
2. W. A. Britton, Y. Chen, F. Sgrignuoli, and L. Dal Negro, ACS Photonics **7**, 2731 (2020).
3. V. Boominathan, J. K. Adams, J. T. Robinson, and A. Veeraraghavan, IEEE Trans. Pattern Anal. Mach. Intell. **42**, 1618 (2020).
4. S. Banerji, M. Meem, A. Majumder, B. Sensale-Rodriguez, and R. Menon, Optica **7**, 214 (2020).
5. D. Lin, A. L. Holsteen, E. Maguid, G. Wetzstein, P. G. Kik, E. Hasman, and M. L. Brongersma, Nano Lett. **16**, 7671 (2016).
6. E. Arbabi, A. Arbabi, S. M. Kamali, Y. Horie, and A. Faraon, Sci. Rep. **6**, 32803 (2016).
7. X. Lin, Y. Rivenson, N. T. Yardimci, M. Veli, Y. Luo, M. Jarrahi, and A. Ozcan, Science **361**, 1004 (2018).
8. M. Veli, D. Mengu, N. T. Yardimci, Y. Luo, J. Li, Y. Rivenson, M. Jarrahi, and A. Ozcan, Nat. Commun. **12**, 37 (2021).
9. Y. Luo, D. Mengu, N. T. Yardimci, Y. Rivenson, M. Veli, M. Jarrahi, and A. Ozcan, Light: Sci. Appl. **8**, 112 (2019).
10. W. A. Britton, Y. Chen, F. Sgrignuoli, and L. Dal Negro, Laser Photonics Rev. **15**, 2000207 (2021).
11. M. Khorasaninejad and F. Capasso, Science **358**, eaam8100 (2017).
12. P. Lalanne and P. Chavel, Laser Photonics Rev. **11**, 1600295 (2017).
13. N. Yilmaz, A. Ozdemir, A. Ozer, and H. Kurt, J. Opt. **21**, 045105 (2019).
14. B. Groever, W. T. Chen, and F. Capasso, Nano Lett. **17**, 4902 (2017).
15. A. Martins, J. Li, B.-H. V. Borges, T. F. Krauss, and E. R. Martins, Nanophotonics **11**, 1187 (2022).
16. E. T. Rogers and N. I. Zheludev, J. Opt. **15**, 094008 (2013).
17. W. Ma, Z. Liu, Z. A. Kudyshev, A. Boltasseva, W. Cai, and Y. Liu, Nat. Photonics **15**, 77 (2021).
18. Z. Liu, D. Zhu, L. Raju, and W. Cai, Adv. Sci. **8**, 2002923 (2021).
19. S. Wang, Y. Teng, and P. Perdikaris, "Understanding and mitigating gradient pathologies in physics-informed neural networks," arXiv:2001.04536 (2020).
20. Y. Chen and L. Dal Negro, APL Photonics **7**, 010802 (2022).
21. G. J. Swanson, "Binary optics technology: the theory and design of multi-level diffractive optical elements," Tech. Rep. 854 (Lincoln Laboratory, Massachusetts Institute of Technology, 1989).
22. M. Gu, *Advanced Optical Imaging Theory*, Vol. 75 (Springer Science & Business Media, 2000).
23. M. Berry and S. Popescu, J. Phys. A: Math. Gen. **39**, 6965 (2006).
24. P. J. S. Ferreira and A. Kempf, IEEE Trans. Signal Process. **54**, 3732 (2006).
25. E. T. Rogers, J. Lindberg, T. Roy, S. Savo, J. E. Chad, M. R. Dennis, and N. I. Zheludev, Nat. Mater. **11**, 432 (2012).